

Supplementary Material for

A facile route to plastic inorganic electrolytes for all-solid state batteries based on molecular design

Insang You^a, Baltej Singh^a, Mengyang Cui^b, Gillian Goward^b, Lanting Qian^a, Zachary Arthur^c,
Graham King^c and Linda F. Nazar^{a*}

^a Chemistry, University of Waterloo, Waterloo, Ontario N2L 3G1, Canada

^b Chemistry, McMaster University, Hamilton, Ontario, L8S 4L8, Canada

^c Canadian Light Source, Saskatoon, SK S7N 2V3, Canada

*Corresponding Author, E-mail: lfnazar@uwaterloo.ca

Supplementary material includes:

Figures S1 to S28

Table S1 to S2

Captions for Movies S1 to S3

Supplementary Figures

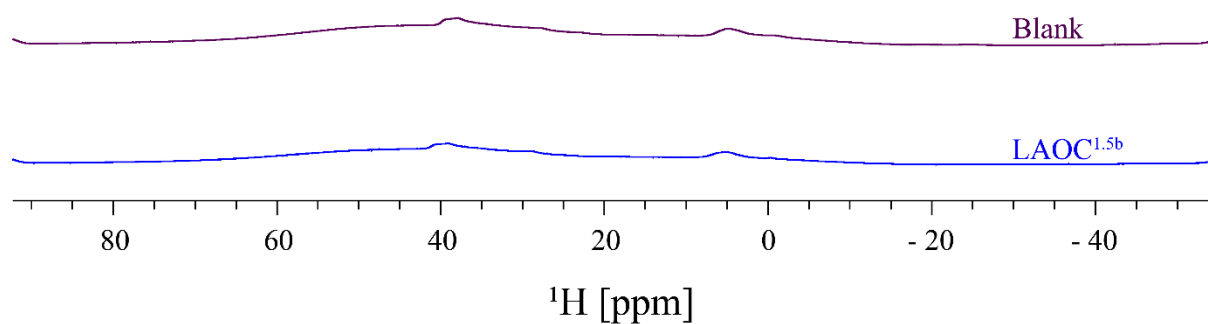


Figure S1. ^1H -ssNMR spectra. ^1H ssNMR signal from LAOC^{1.5b} and background showing that they are the same; thus all the introduced H_2O was decomposed and the HCl gas produced was fully evaporated during synthesis. The magnetic field strength was 20 T.

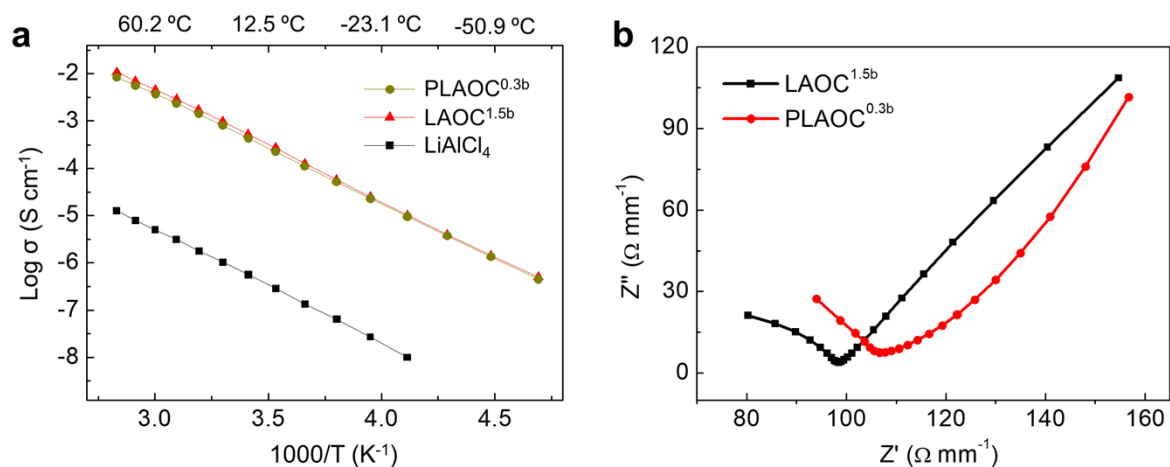


Figure S2. Ionic conductivity of LAOC^{1.5b} and PLAOC^{0.3b}. (a) Arrhenius plots for LAOC^{1.5b}, PLAOC^{0.3b} and LiAlCl₄. The superscript of LAOC^x denotes the number of bridging Cl, and PLAOC refers to LAOC plasticized by the additional incorporation of LiAlCl₄. The ionic conductivity of LAOC increased about 10³-fold compared to LiAlCl₄ while the activation energy of LAOC^{1.5b} (0.471 eV) and PLAOC^{0.3b} (0.460 eV) are comparable to LiAlCl₄ (0.475 eV). The activation energy values were calculated from the temperature range from -60 °C to 70 °C. (b) Nyquist plots for LAOC^{1.5b} and PLAOC^{0.3b}. Impedance was normalized by their thickness (area: 0.785 cm²).

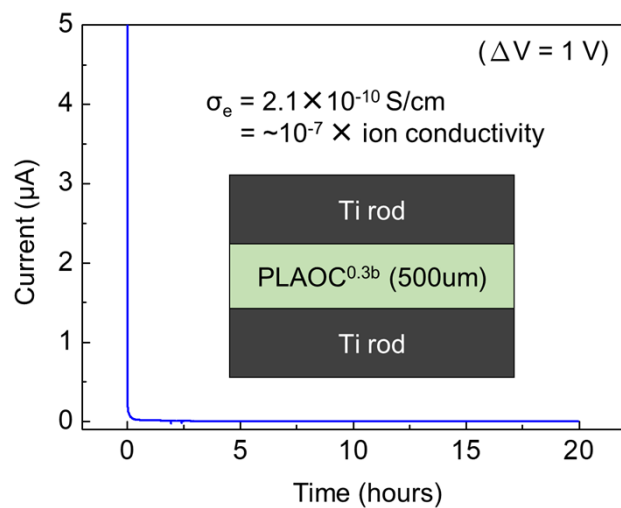


Figure S3. Electrical polarization protocol for determining the electrical conductivity of PLAOC^{0.3b}. The conductivity was measured after 20 hours of DC polarization ($\Delta V=1 \text{ V}$).

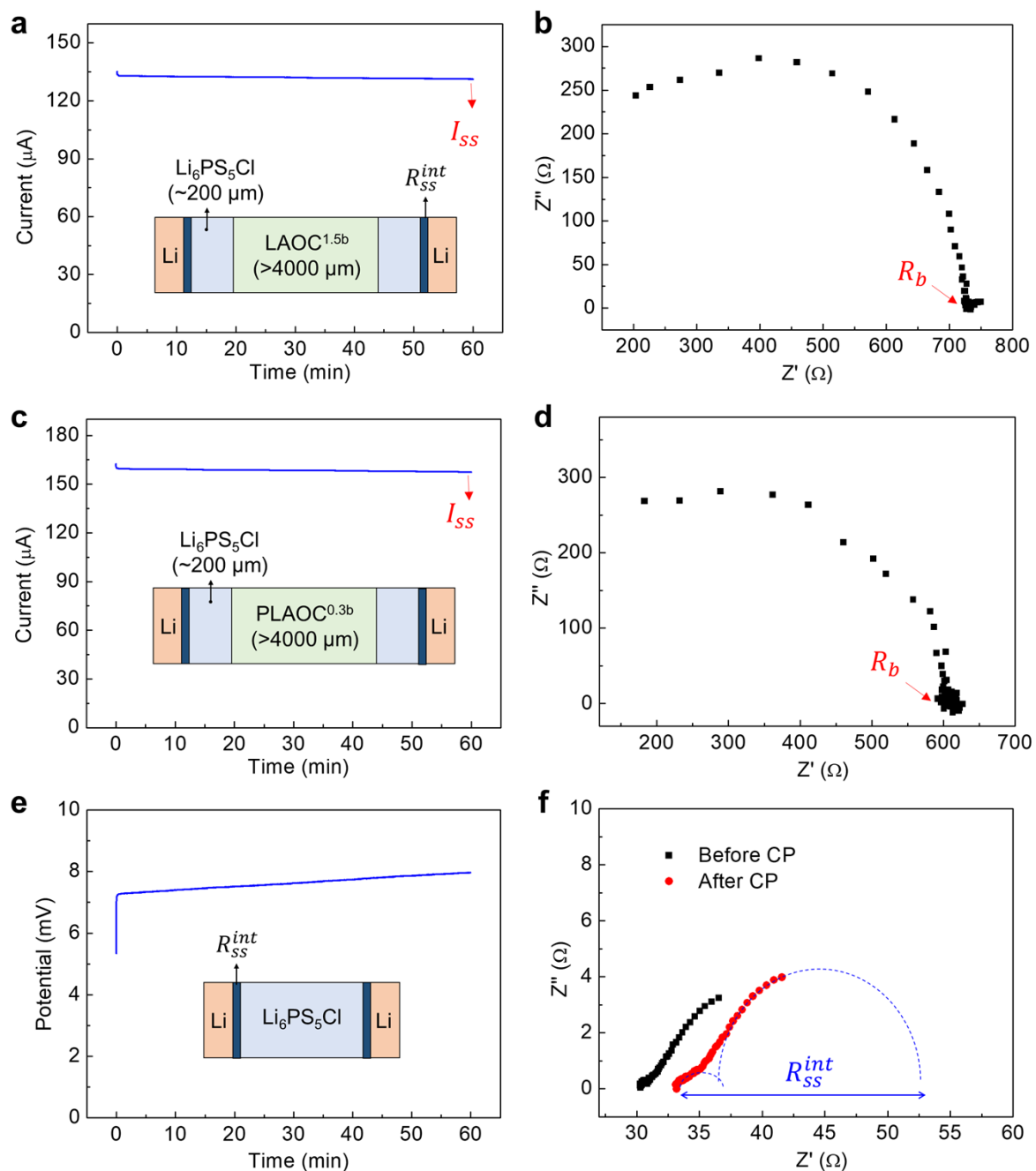


Figure S4. Li^+ transference number determination. (a) Chronoamperometry (CA) ($\Delta V=100$ mV) of a Li-symmetric LAOC^{1.5b} cell. (b) Nyquist plot of cell (a) measured by potentiostatic electrochemical impedance spectroscopy (PEIS) after the CA study. (c) CA ($\Delta V=100$ mV) of a Li-symmetric PLAOC^{0.3b} cell. (d) Nyquist plot of cell (c) measured by PEIS after the CA study. (e) Chronopotentiometry (CP) ($\Delta I=150 \mu\text{A}$, comparable to I_{ss}) of a Li-symmetric $\text{Li}_6\text{PS}_5\text{Cl}$ cell. (f) Nyquist plot of cell (e) measured by PEIS before and after the CP study. The continuous potential increase in (e) is attributed to the reaction between $\text{Li}_6\text{PS}_5\text{Cl}$ and Li metal which induced the resistance increase shown in (f).

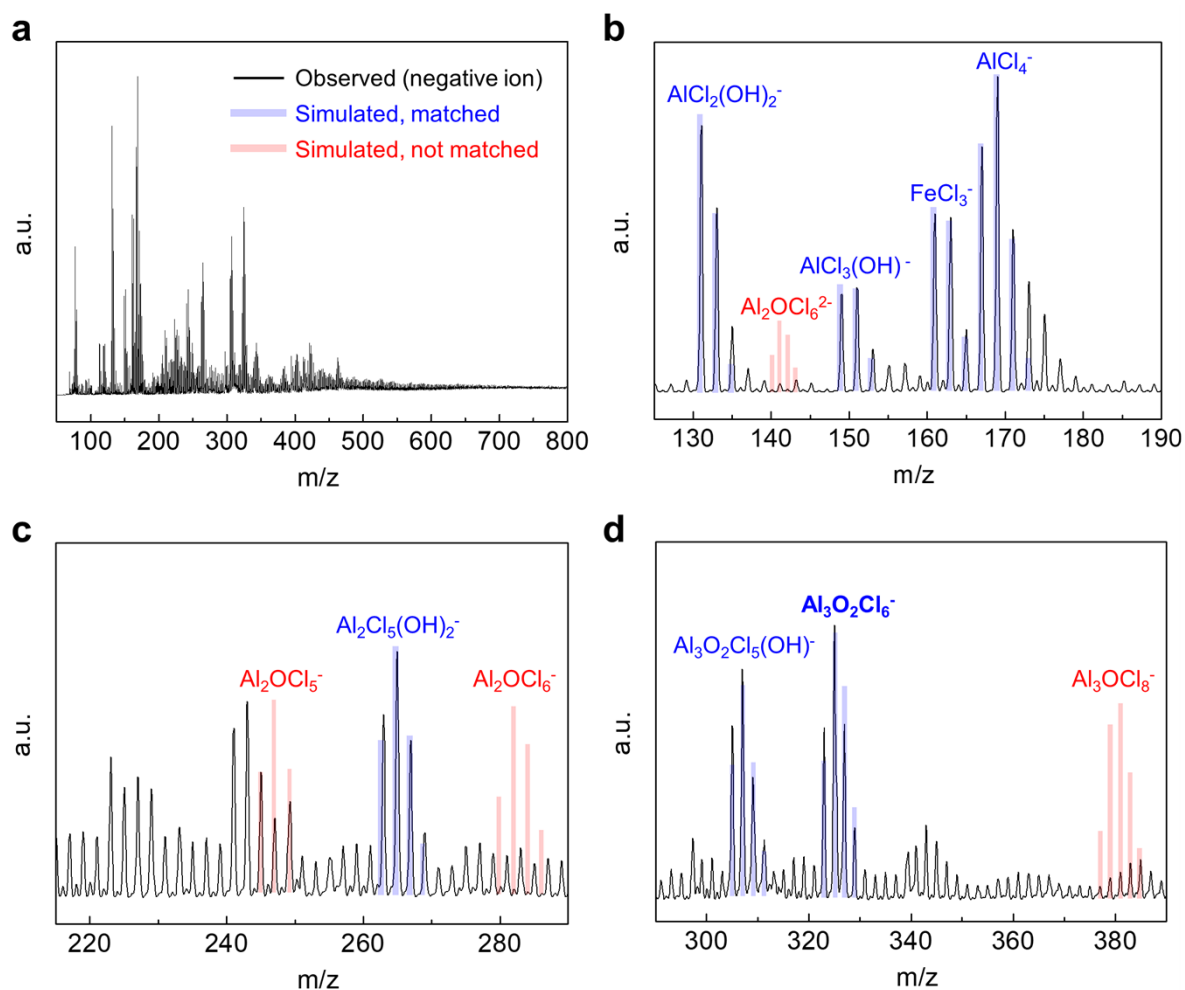


Figure S5. Electro spray ionization (negative-ion) mass spectrometry (ESI-MS). (a) Observed negative-ion mass spectrum in the entire m/z range - peak intensities do not quantitatively reflect the fraction of the anion in solution; (b) Magnified spectrum in the m/z range of 130 to 190 that corresponds to anionic monomers – note that FeCl_3 is a typical impurity in the reagent AlCl_3 ; (c) Magnified spectrum in the m/z range of 200 to 290 that corresponds to anionic dimers. (d) Magnified spectrum in the m/z range of 300 to 390 that corresponds to anionic trimers. The black curve denotes the observed spectrum. Blue and red curves denote the simulated spectrum. The simulated spectrum of each oligomer shows three to five consecutive m/z peaks, separated by $m/z=2$ (monovalent) or 1 (divalent), due to chlorine isotopes. Small peaks in the background come from the fragmented chlorine.

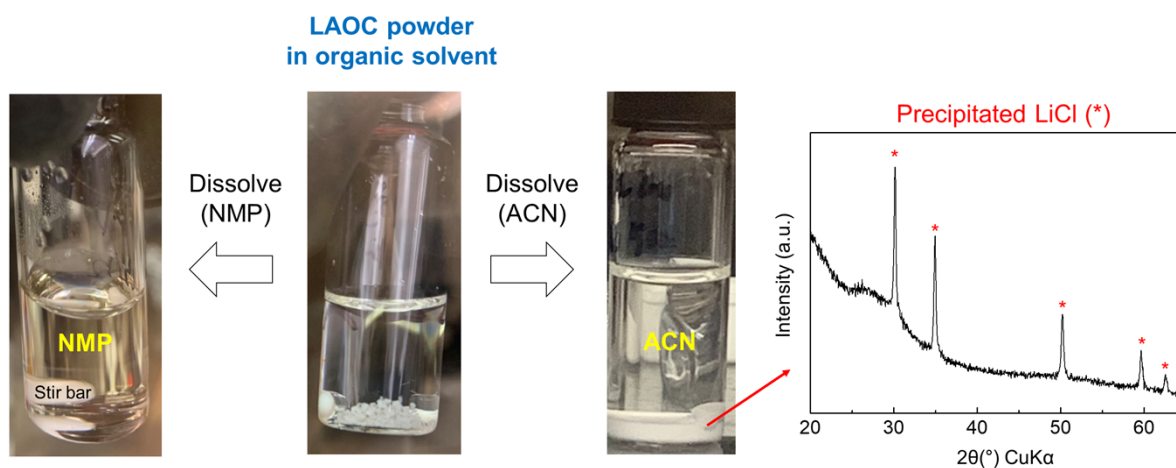


Figure S6. Dissolution of LAOC powder in organic solvents and XRD of precipitated LiCl. Oligomeric LAOC has a discrete molecular structure, so it can be dissolved in polar organic solvents. Anionic oligomers convert into monovalent $\text{Al}_3\text{O}_2\text{Cl}_6^-$, thus releasing LiCl. Consequently, LiCl precipitates in acetonitrile (ACN) due to its low solubility in ACN, whereas LAOC can be completely dissolved in N-Methyl-2-pyrrolidone (NMP), resulting in a transparent solution. The LAOC-ACN solution prepared for ESI mass spectroscopy was transparent due to its low concentration of oligomer ($50 \mu\text{mol/L}$). We note that NMP is not suitable as a solvent for ESI-MS.

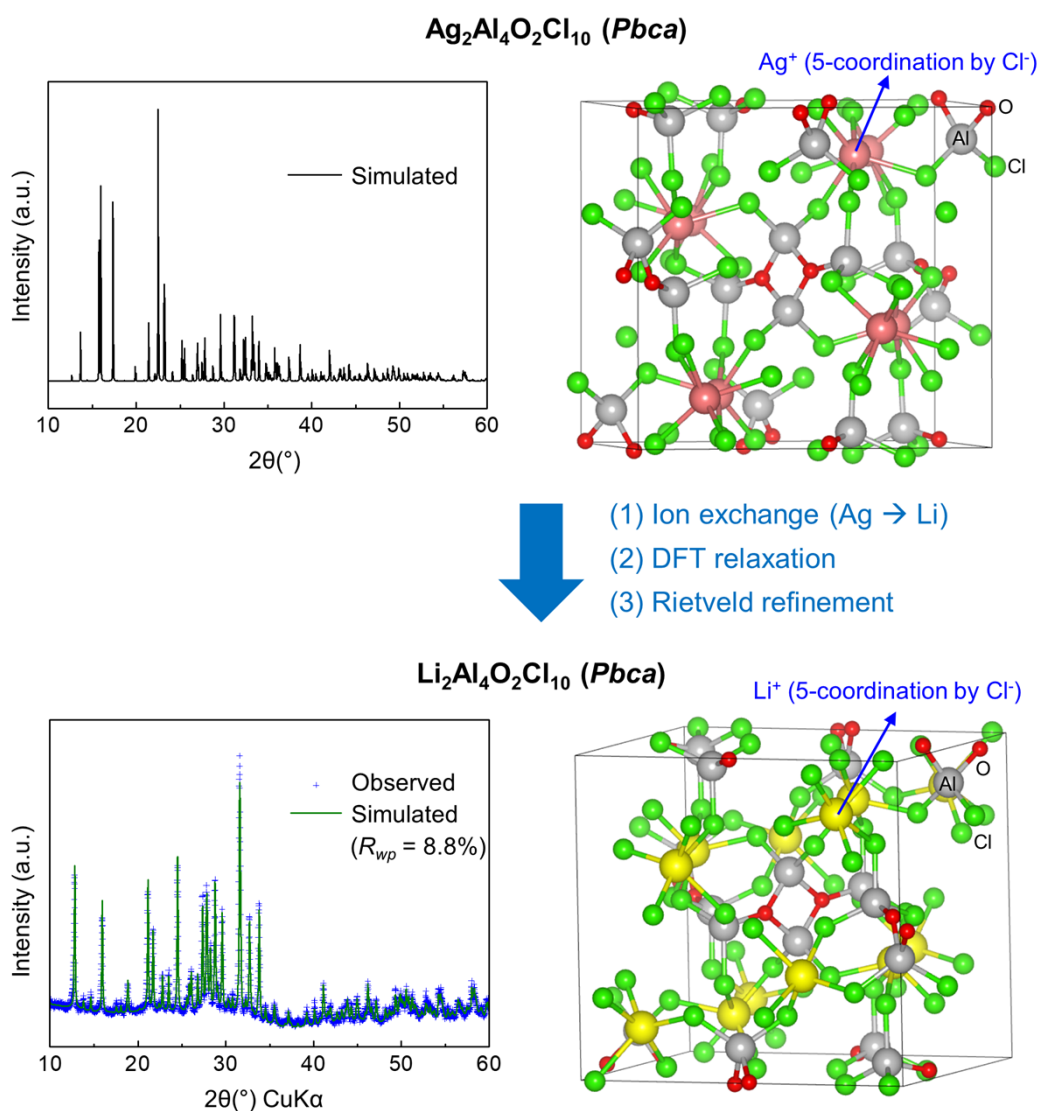


Figure S7. XRD pattern and crystal structure of Li₂Al₄O₂Cl₁₀ derived from Ag₂Al₄O₂Cl₁₀. (a) Ag₂Al₄O₂Cl₁₀ crystal structure (*Pbca*) and simulated diffraction pattern. (b) Rietveld refinement of Li₂Al₄O₂Cl₁₀ (green curve) using the DFT-relaxed structure against the experimental XRD data (blue crosses). *R*_{wp} is the weighted profile R-factor. The structure after refinement is shown in the right panel.

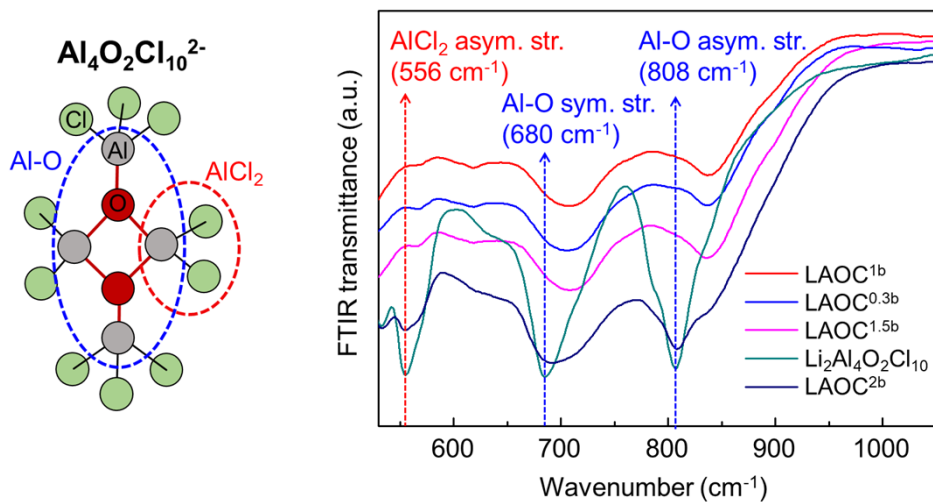


Figure S8. FTIR spectroscopy for different lithium aluminum oxychlorides. The existence of $\text{Li}_2\text{Al}_4\text{O}_2\text{Cl}_{10}$ was verified based on three characteristic peaks in its FTIR spectrum at 556, 680 and 808 cm^{-1} . While LAOC^{2b} is a mixed phase with $\text{Li}_2\text{Al}_4\text{O}_2\text{Cl}_{10}$, as the degree of saturation increases from $\text{LAOC}^{1.5b}$ to $\text{LAOC}^{0.3b}$, the three characteristics peaks from $\text{Al}_4\text{O}_2\text{Cl}_{10}^{2-}$ disappear.

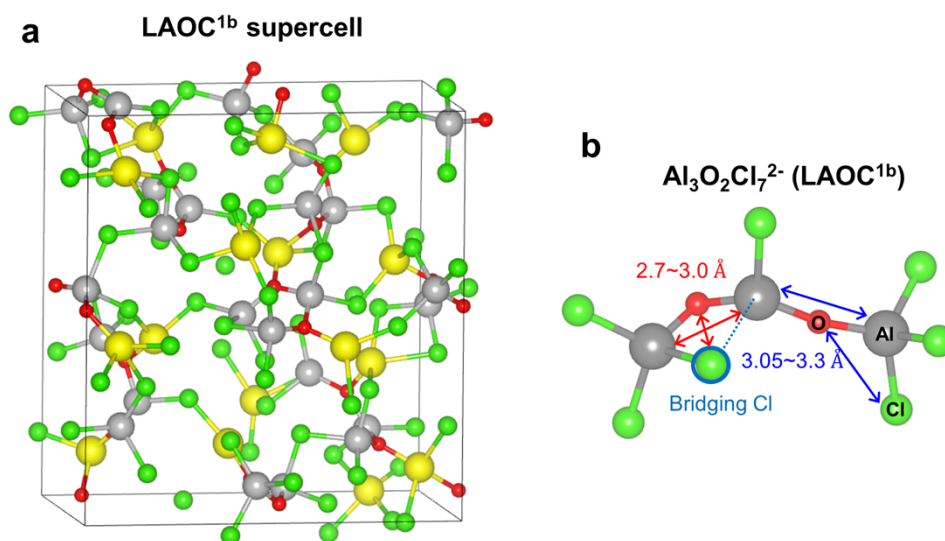


Figure S9. AIMD-simulated models for LAOC^{1b}. (a) Simulated LAOC^{1b} supercell after melt-quenching at 600 K. Eight LAOC^{1b} oligomers are distributed in the supercell. (b) Anionic trimer for LAOC^{1b}. The distance range between Al-Al^{1st} and O-Cl^{1st} with bridging Cl is noted in red. The distance range between Al-Al^{1st} and O-Cl^{1st} without bridging Cl is noted in blue.

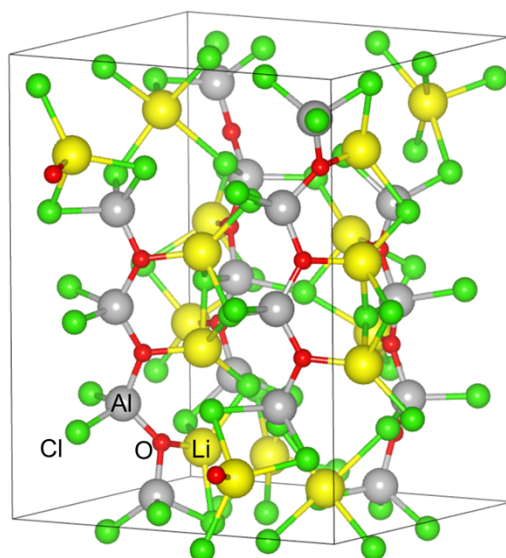


Figure S10. Simulated structure model for LAOC tetramer. The supercell was constructed by distributing the tetramer ($\text{Li}_4\text{Al}_4\text{O}_3\text{Cl}_{10}$) which is formed by adding one more aluminum, bridged by oxygen, to the trimer. The calculated energy above hull of this structural model is 365.9 meV/atom.

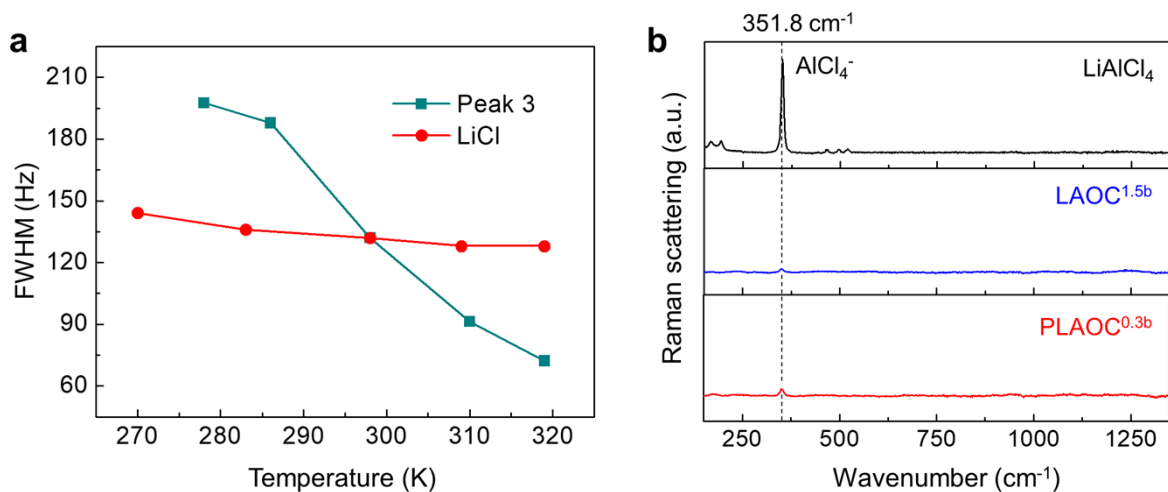


Figure S11. (a) Full-width-half-maximum (FWHM) comparison of the ssNMR peak from solid LiCl and Peak 3 from LAOC^{1.5b} at different temperatures. The FWHM of Peak 3 changes with a much larger amplitude compared to that of LiCl. This implies that Li[Cl₆] in LAOC^{1.5b} is in a more dynamic state compared to Li[Cl₆] in LiCl, demonstrating their different nature. **(b)** Raman spectroscopy of LiAlCl₄, LAOC^{1.5b} and PLAOC^{0.3b}. LiAlCl₄ shows a major peak at 351.8 cm⁻¹ that mostly disappears in LAOC^{1.5b}. In PLAOC^{1.5b}, with the additionally incorporated LiAlCl₄, the peak is slightly more pronounced.

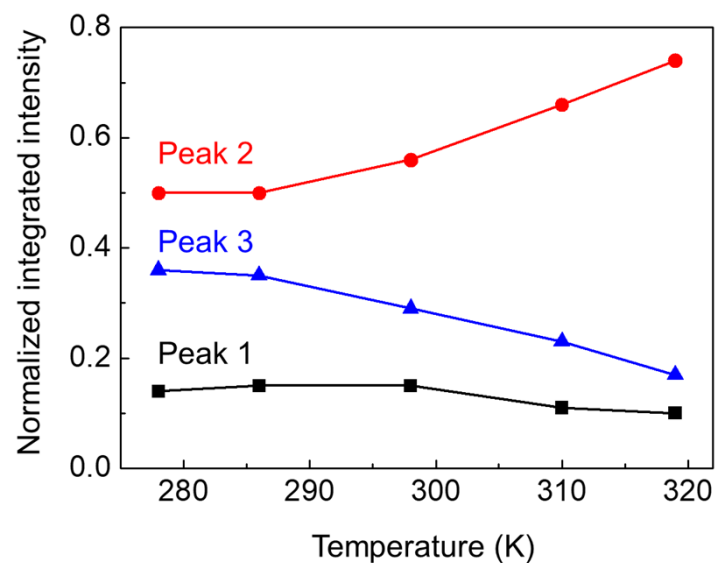


Figure S12. Normalized integrated intensity of Peaks (1-3) in ^7Li ssNMR of LAOC^{1.5b}. Integrated intensity of ^7Li ssNMR peaks from 278 K to 319 K. The value for Peak 2 increased from 0.5 to 0.75 while the values for Peak 1 and 3 decreased.

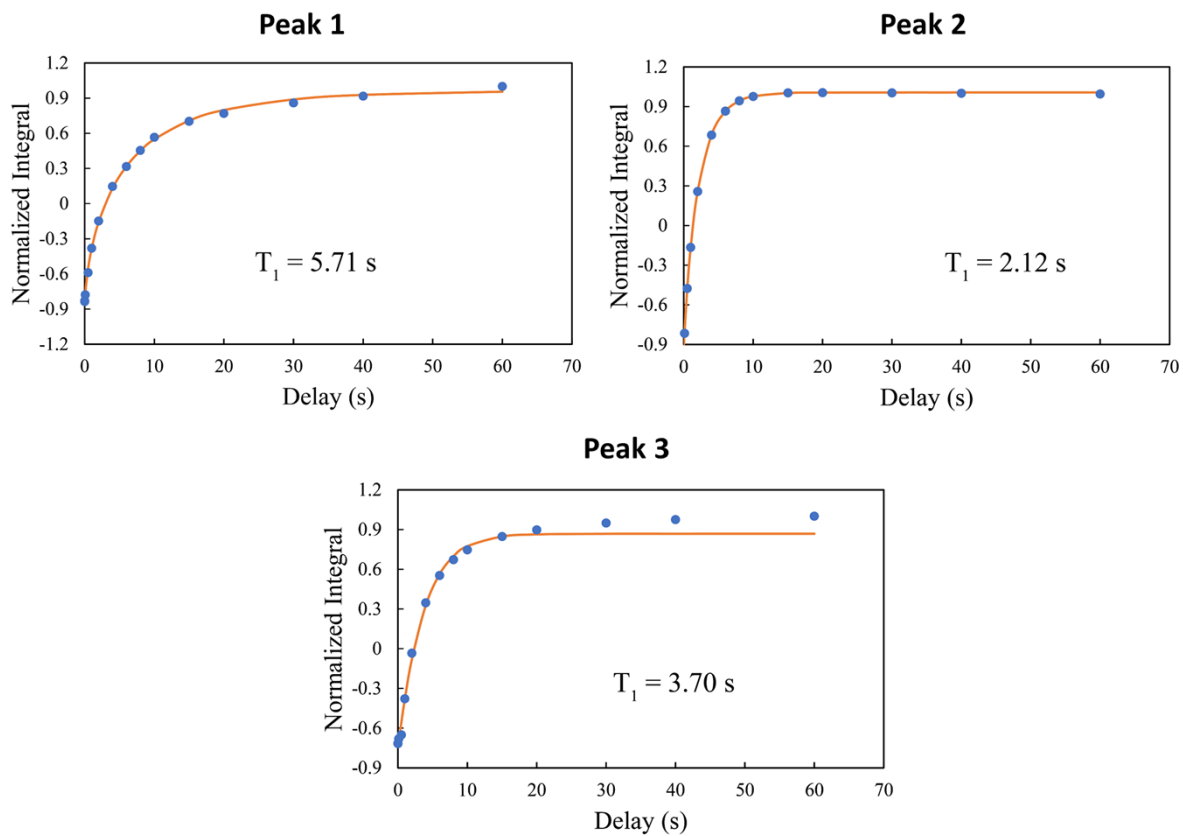


Figure S13. T_1 relaxation time of Peaks (1-3) in the ^7Li ssNMR of LAOC^{1.5b} at 309 K. The relaxation time fit from Peak 2 (2.12 s) is smaller than the values fit from Peak 1 (5.71 s) and Peak 3 (3.70 s).

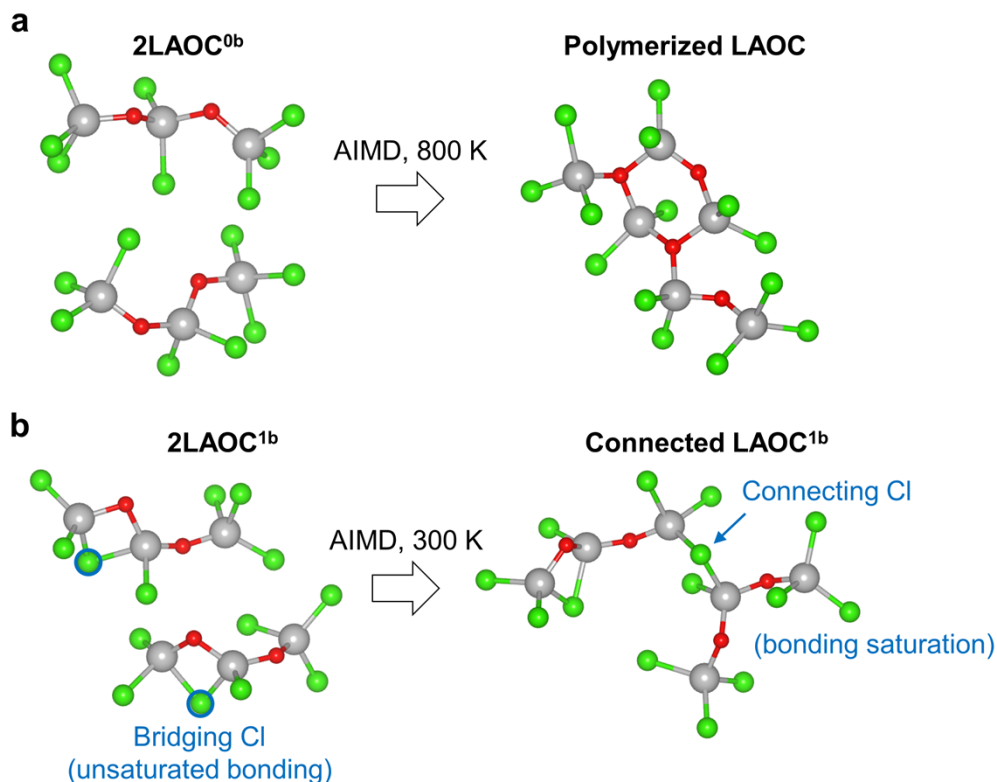


Figure S14. Configurational stability of LAOC^{1b} and LAOC^{0b} observed during AIMD simulation
(a) LAOC^{1b} that contains bridging Cl (unsaturated bonding) can be connected to other LAOC^{1b} oligomers through Al-Cl-Al bonding. During AIMD simulation, some of LAOC^{1b} in the supercell became connected even at 300 K. It implies that unsaturated LAOC would contain oligomers connected by bridging Cl. **(b)** LAOC^{0b} does not show any further connection during AIMD simulation at 300 K, while it started to polymerize at 800 K as the consequence of thermal decomposition. We note that Al-Cl-Al connections are considered as weaker (and likely reversible) bonding compared to Al-O-Al polymerization.

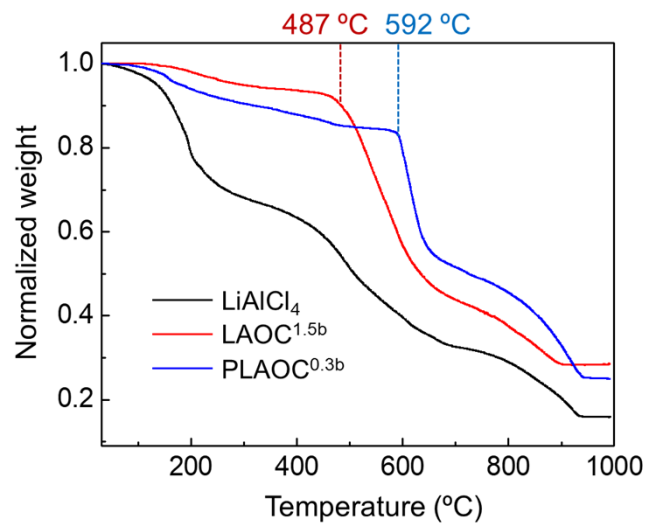


Figure S15. TGA analysis for LiAlCl₄ and LAOC. TGA was conducted up to 1000 °C to determine the decomposition temperature under N₂. The degradation temperatures for LAOC^{1.5b} (487 °C) and PLAOC^{0.3b} (592 °C) are much higher than LiAlCl₄ (180 °C). PLAOC^{0.3b} exhibited mass loss before the degradation point, which is expected due to the decomposition of the added LiAlCl₄.

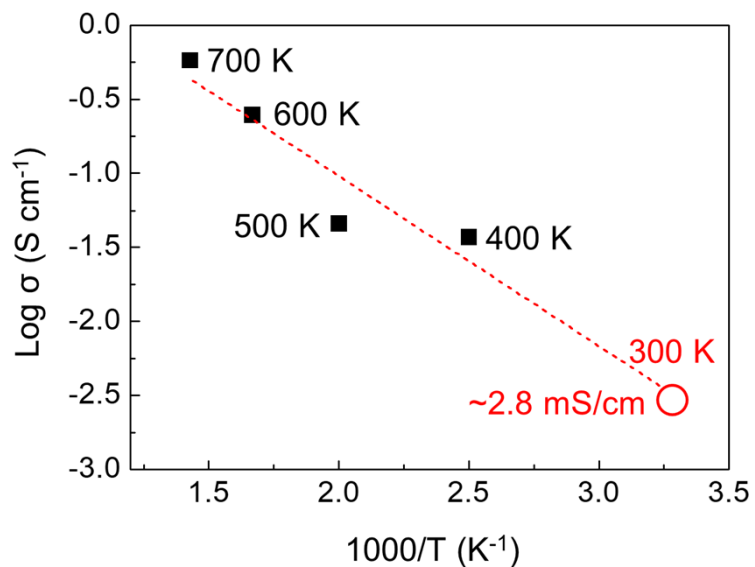


Figure S16. Calculated Li conductivity of LAOC^{0b} model through AIMD simulation. Li conductivity was calculated based on the analysis of Li MSDs. AIMD simulations at each temperature were performed for 100 ps in the NVT ensemble with the experimental density of LAOC (1.9 g/cm³). Conductivity at 300 K was obtained by extrapolating the values measured at higher temperatures (400-700 K). AIMD simulation at 800 K results in thermal decomposition of LAOC^{0b}, so 700 K is the maximum accessible temperature.

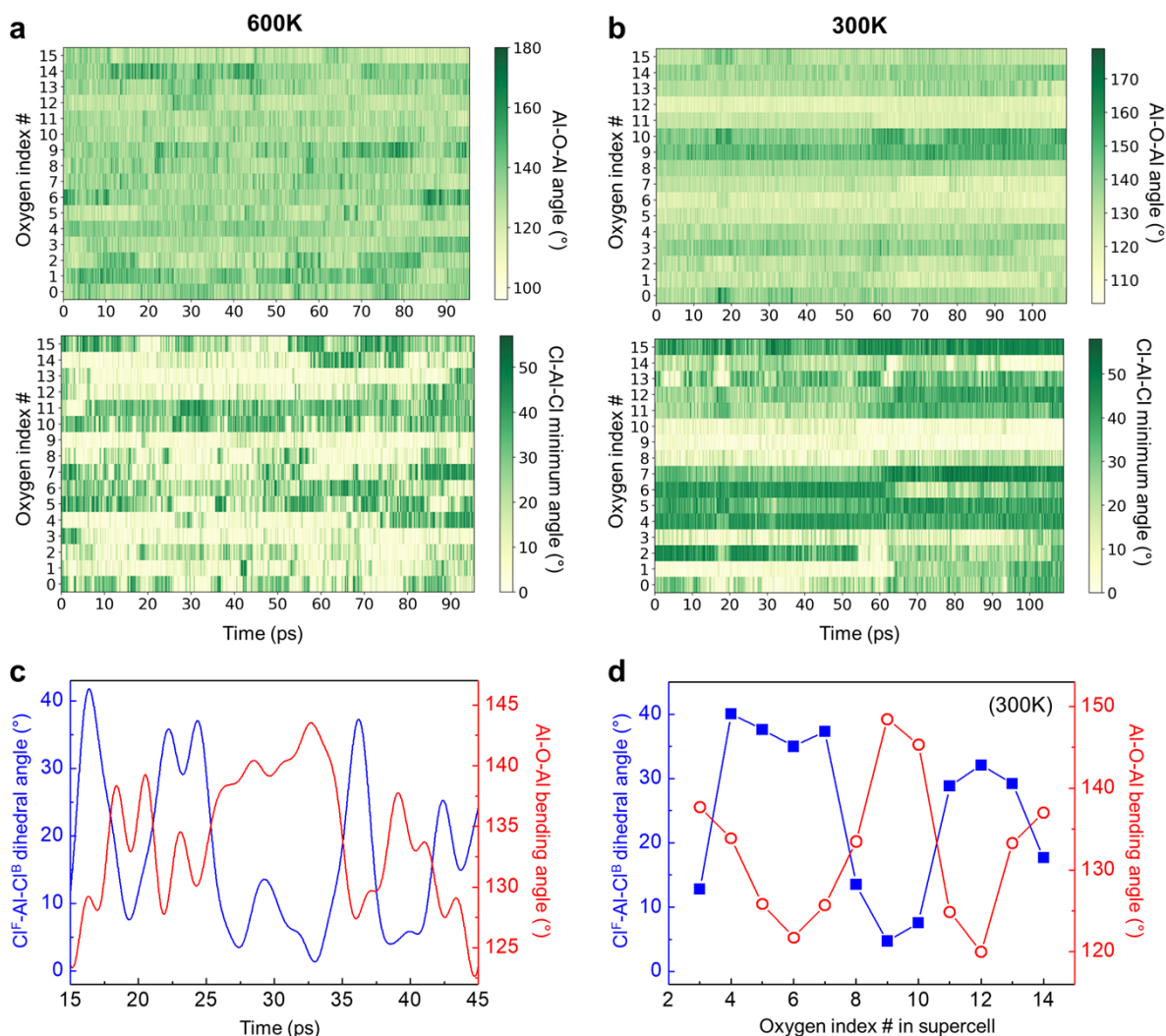


Figure S17. Characteristic angles of LAOC^{0b} during AIMD simulation (a,b) Heat map presenting Al-O-Al bending angle (top) and Cl^F-Al-Cl^B dihedral angle (bottom) of LAOC^{0b} during AIMD simulation at 600 K (a) and 300K (b). Each angle was calculated based on oxygen as a geometric reference point. The supercell contains sixteen oxygens (two oxygens in each LAOC^{0b}) from eight LAOC^{0b} trimers. Notable angle variation was observed in the heat map at 600 K. Oxygen #0 is displayed in Fig. 4e (bottom) as an example. The 300 K heat map showed less frequent angles change compared to the 600 K heat map. Oxygen #1 is displayed in Fig. 4e (top) as an example. **(c)** Characteristic angle variations observed during AIMD simulation at 600 K. When LAOC^{0b} is bent, the distance between Cl^F and Cl^B decreases, inducing steric hindrance that favors a staggered conformation. Conversely, an eclipsed conformation is allowed when LAOC^{0b} becomes flat as the Cl ions recede. Thus, the two characteristic angles are inversely correlated, as shown in the plot. **(d)** Averaged characteristic angles over 100 ps from 300 K heat maps. The characteristic angles show limited dynamics at 300 K, so the average values approximately represent their static conformation. The plot indicates that the two angles are inversely correlated in the static state.

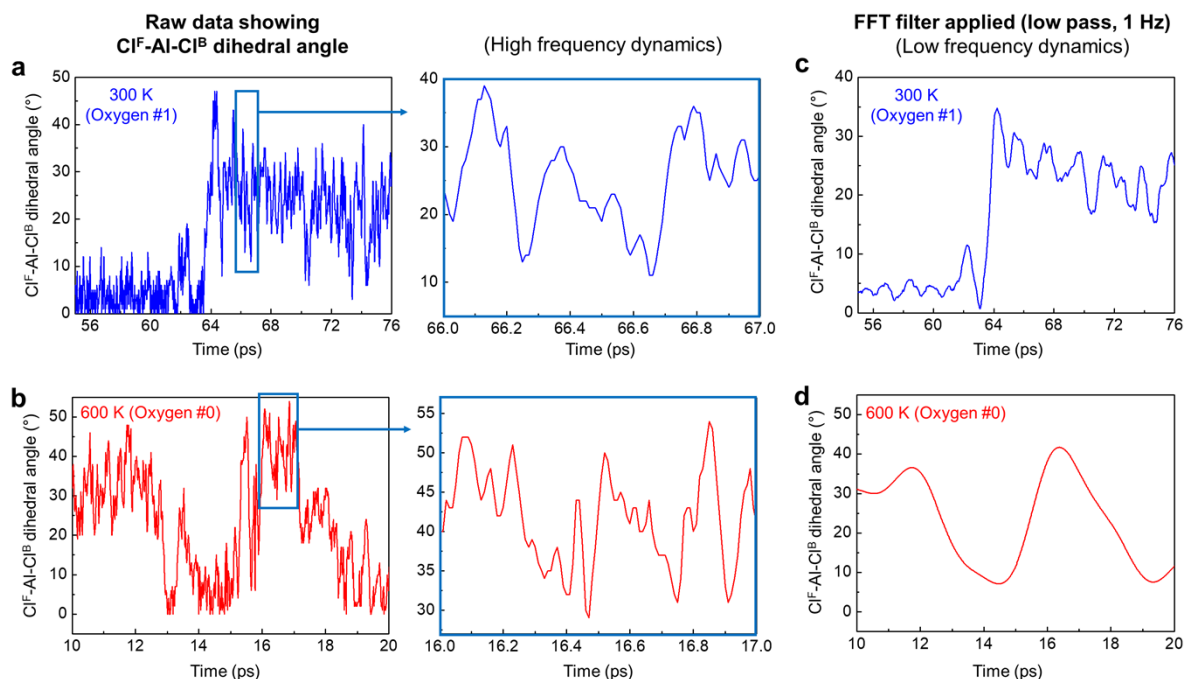


Figure S18. Dihedral angle variations in different frequency ranges. (a, b) Raw data for observed dihedral angles during AIMD simulation at 300 K (a) and 600 K (b). The high-frequency dynamics, corresponding to vibrational motion, are observed in magnified plots (right panels). **(c, d)** Observed dihedral angle after applying an FFT filter (low pass, 1 Hz) to capture low-frequency dynamics corresponding to rotational motion at 300 K (c) and 600 K (d). Rotational motion exhibited a frequency range between THz (ps^{-1}) and GHz (ns^{-1}), whereas vibrational motion occurred at frequencies higher than THz (ps^{-1}).

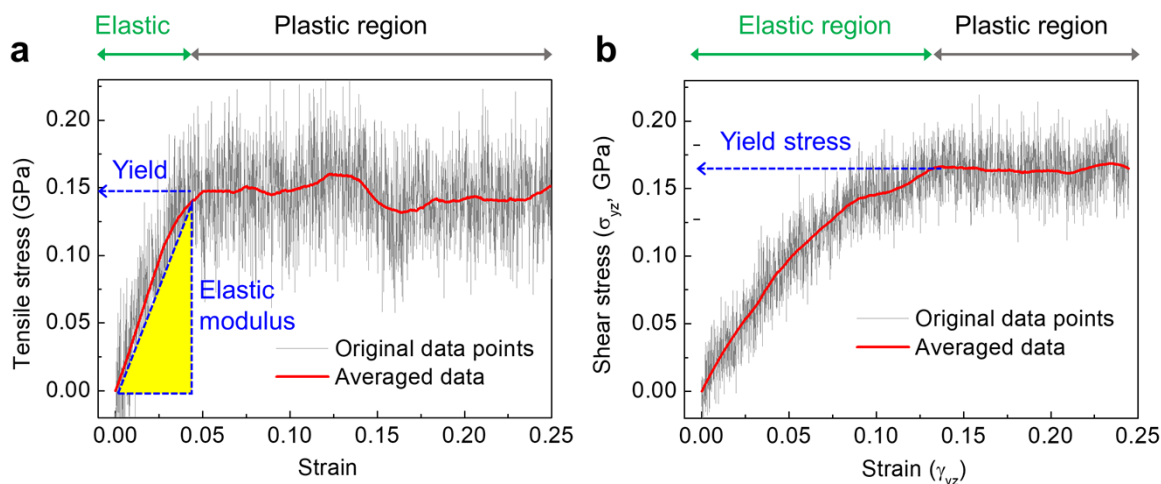


Figure S19. Calculated stress-strain response curve of LAOC^{0b} structure model using the DeepMD potential. (a) Stress-strain curve response to tensile stress in the x-axis; the slope in the elastic region provides a calculated modulus of ~ 3 GPa; **(b)** Stress-strain curve response to shear stress in the yz-plane. The strain was applied at a rate of 10^{-3} ps⁻¹ using the DeepMD potential model in molecular dynamics simulations at 300 K.

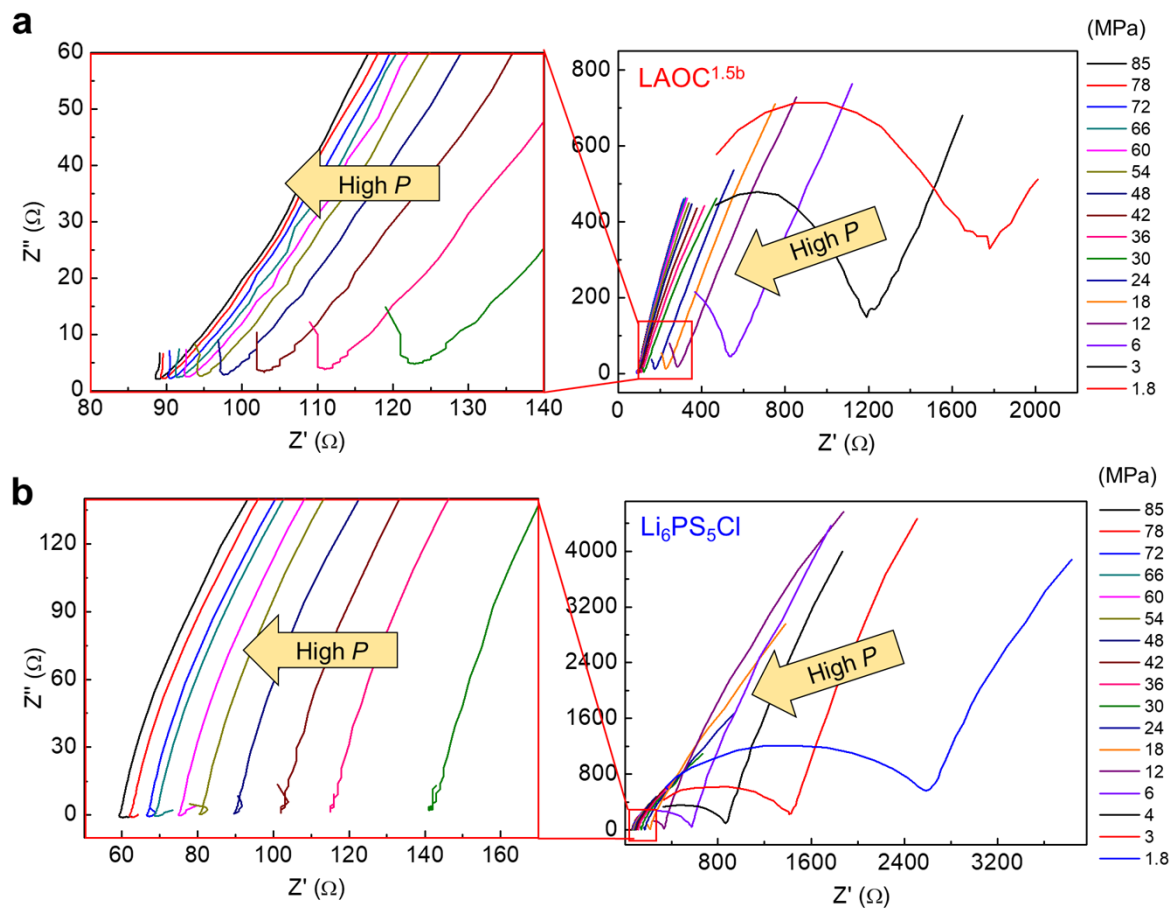


Figure S20. Ion conductivity analysis of SSE as a function of pressure. (a, b) Nyquist plots of LAOC^{1.5b} (a) and Li₆PS₅Cl (b) as a function of pressure from 1.8 MPa to 85 MPa. Magnified images are displayed in left panels to depict the plots at high pressure.

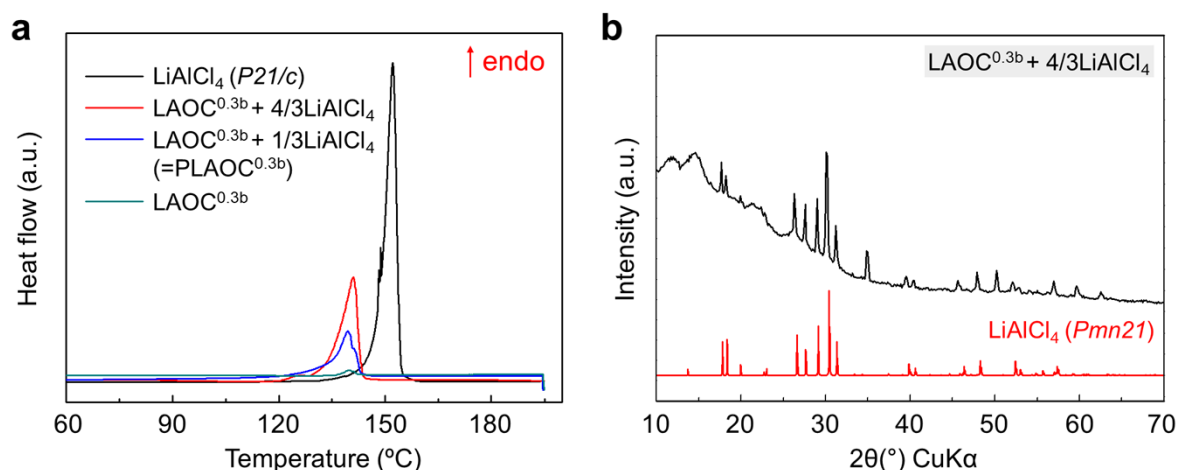


Figure S21. DSC trace and XRD patterns for LiAlCl_4 -incorporated $\text{LAOC}^{0.3b}$. (a) DSC curves for LiAlCl_4 , $\text{LAOC}^{0.3b}$ and plasticized $\text{LAOC}^{0.3b}$. The peak at 152 °C corresponds to melting of LiAlCl_4 in the *P21/c* phase and the peak at 141 °C corresponds to melting of the *Pmn21* LiAlCl_4 phase. The intensity of these peaks was negligible in $\text{LAOC}^{0.3b}$, indicating a very minimal amount of residual LiAlCl_4 . The intensity of the peak obviously increases with additional LiAlCl_4 (red trace). The peak in PLAOC^{0.3b} (blue trace) indicates that LiAlCl_4 is dissolved in it, although LiAlCl_4 is not observed in the XRD pattern. Heat flow was normalized by sample weight. (b) XRD pattern of plasticized $\text{LAOC}^{0.3b}$ having an excess fraction of LiAlCl_4 , much larger than the fraction in PLAOC^{0.3b}. After synthesis, the excess LiAlCl_4 phase-separates as the *Pmn21* phase, different from the pristine phase (*P21/c*). The simulated diffraction pattern of LiAlCl_4 (*Pmn21*) is displayed in red.

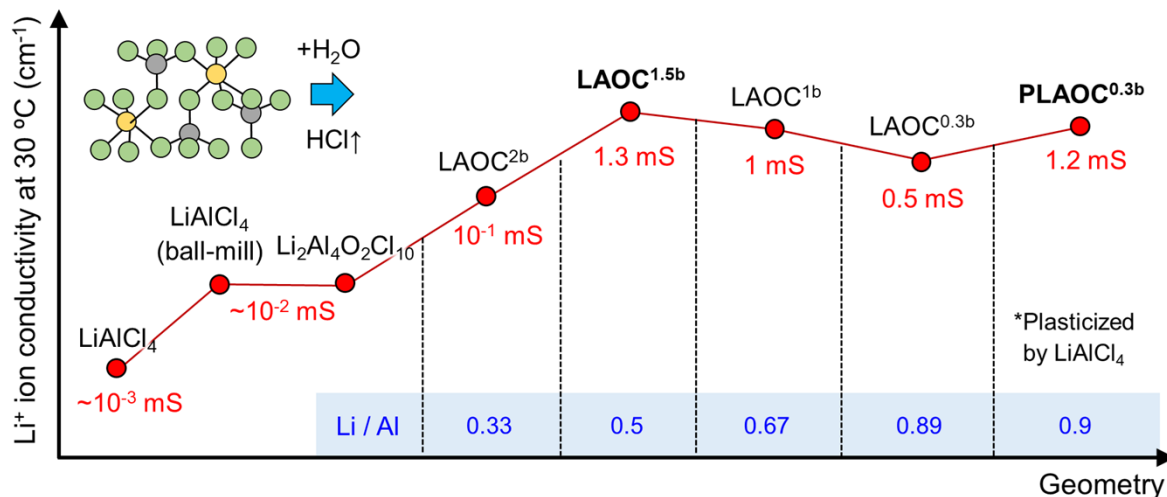


Figure S22. Li⁺ ion conductivity as a function of the structural evolution of solid-state chloroaluminates and oxychlorides. The representative oligomer is displayed in each LAOC composition. LAOC^{1.5b} and PLAOC^{0.3b} demonstrated the highest conductivity with minimal phase separation of LiCl. The inset scheme shows the crystal structure of LiAlCl₄.

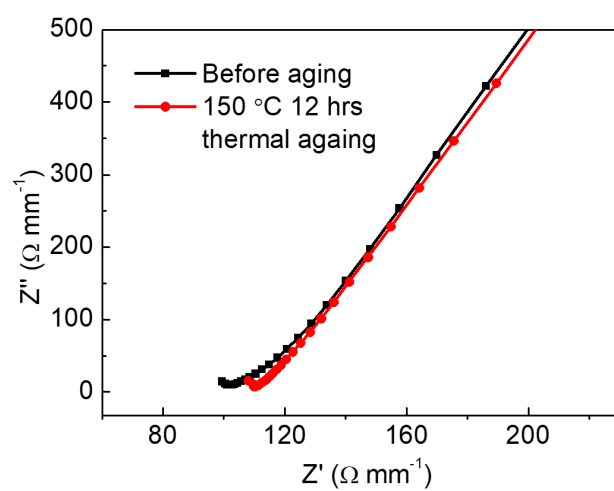


Figure S23. Impedance spectroscopy of LAOC^{1.5b} before and after thermal aging at 150 °C for 12 hours.

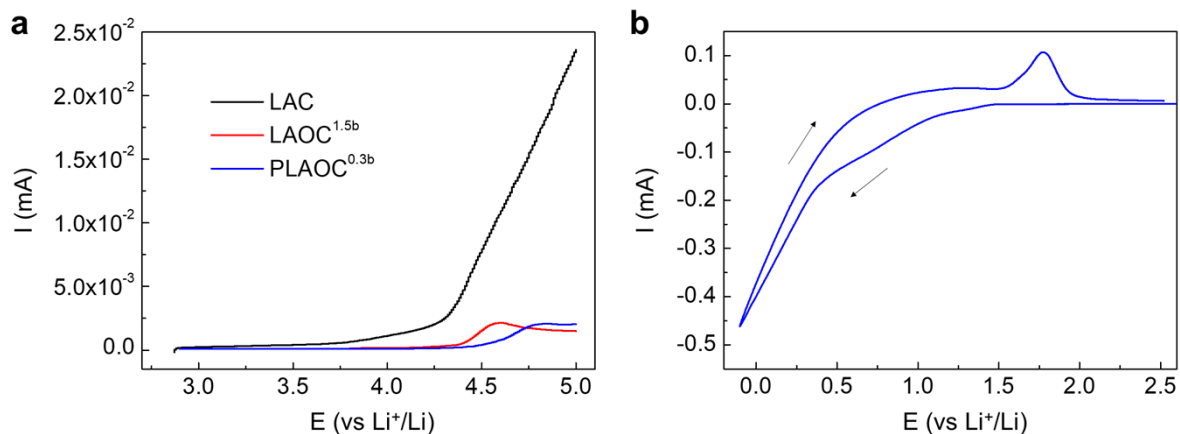


Figure S24. Linear sweep voltammetry (LSV) and cyclic voltammetry (CV) for determining electrochemical stability of LAOC. (a) LSV showing anodic reaction of cathode composite consists of LAC (or LAOC) (95 wt%) and Super P (5 wt%). **(b)** CV showing the cathodic reaction of PLAOC^{0.3b} due to the reduction of Al³⁺ to Al metal (~1.4 V vs Li⁺/Li). It is notable that the cathodic current of PLAOC^{0.3} is 100-fold larger than the anodic current.

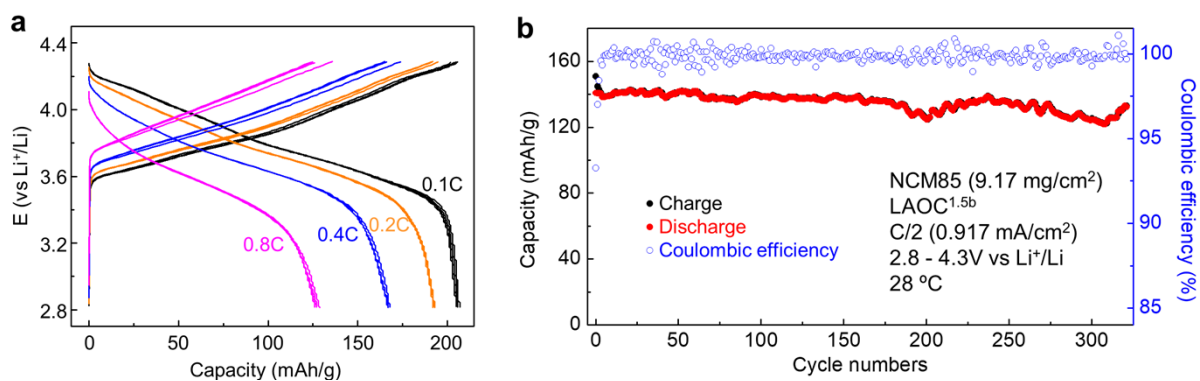


Figure S25. Electrochemical properties of LAOC. (a) Rate capability test of ASSB with PLAOC^{0.3b} at 28 °C with an upper cutoff voltage of 4.3 V – the first five cycles are shown at each rate; **(b)** Cycling profile of an ASSB whose cathode composite consisted of NCM85 and LAOC^{1.5b} (80:20).

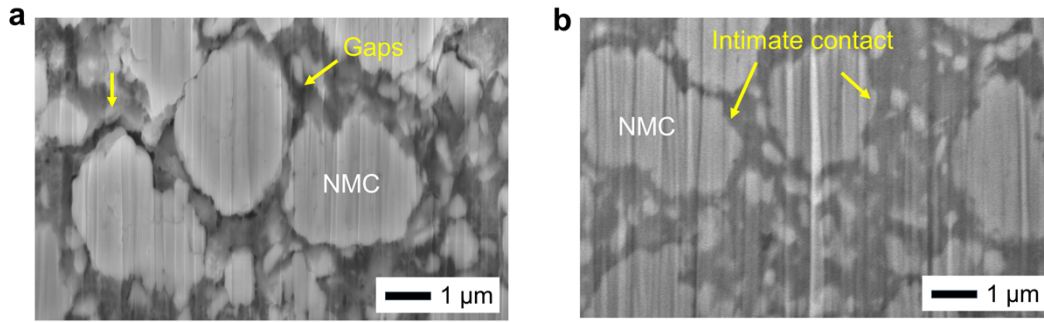


Figure S26. Cross-sectional SEM images prepared by focused ion beam milling of cathode composites. (a) Cathode composite consisting of NMC and LiAlCl_4 . **(b)** Cathode composite consisting of NMC and $\text{PLAOC}^{0.3b}$. The cathode composites were pressed at 200 MPa of uniaxial pressure for 3 mins.

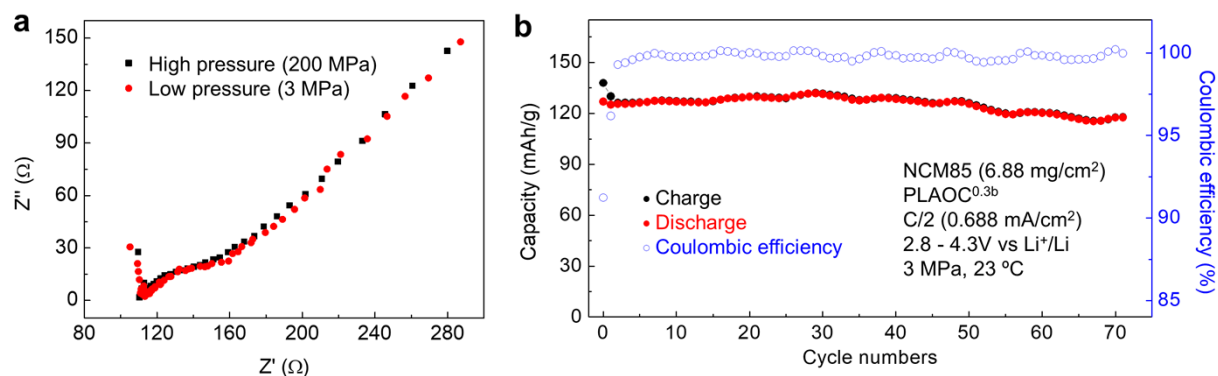


Figure S27. Electrochemical properties for low-pressure ASSB cell. (a) Impedance spectroscopy of the ASSB cell at high and low pressure. **(b)** Charge-discharge capacity of the ASSB cell operated under low pressure (3 MPa). The cathode composite comprised NMC85 and PLAOC^{0.3b} (70:30 wt%).

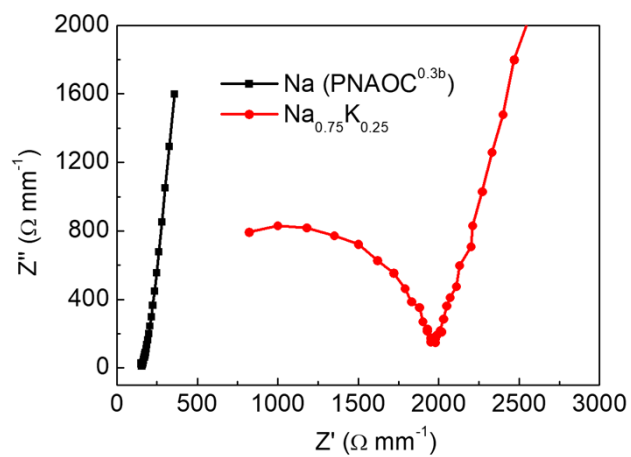


Figure S28. Conductivity of sodium-based aluminum oxychloride. Nyquist plots for plasticized Na-AOC^{0.3b} and plasticized Na_{0.75}K_{0.25}-AOC^{0.3b} at 30 °C. The impedance was normalized by thickness (area: 0.785 cm²).

	LAOC ^{1.5b}	PLAOC ^{0.3b}
ΔV	100 mV	100 mV
I_{ss}	131 μ A	157 μ A
R^b	731 Ω	610 Ω
R_{ss}^{int}	19.3 Ω	19.3 Ω
$t_{Li^+} \left(\frac{I_{ss}R^b}{\Delta V - I_{ss}R_{ss}^{int}} \right)$	0.982	0.989

Table S1. Li transference number calculation. Li transference numbers for LAOC^{1.5b} and PLAOC^{0.3b} were calculated based on the Watanabe method. The observed values utilized for the calculation are shown in the table.

$a = 11.1144(3) \text{ \AA}$, $b = 12.0569(3) \text{ \AA}$, $c = 12.7748(4) \text{ \AA}$, Space group: <i>Pbca</i>						
Atom	Wyckoff site	x	y	z	Occupancy	$U_{\text{iso}} (\text{\AA}^2)$
Li1	8 c	-0.001(5)	0.164(4)	0.811(3)	1	0.04
Al1	8 c	0.0125(9)	0.6075(6)	0.9934(8)	1	0.025(3)
Al2	8 c	0.2085(7)	0.0451(6)	0.3540(7)	1	0.0196(29)
Cl1	8 c	0.0532(6)	0.2095(6)	0.6275(6)	1	0.0127(27)
Cl2	8 c	0.1120(7)	0.6989(6)	0.1057(6)	1	0.034(3)
Cl3	8 c	0.1213(6)	0.0110(7)	0.9153(4)	1	0.0205(23)
Cl4	8 c	0.1690(5)	0.5294(6)	0.7087(5)	1	0.0218(25)
Cl5	8 c	0.2147(7)	0.2250(6)	0.3540(4)	1	0.0255(25)
O1	8 c	0.0979(13)	0.0122(16)	0.4447(10)	1	0.025

Table S2. Lattice parameters and atomic coordination of $\text{Li}_2\text{Al}_4\text{O}_2\text{Cl}_{10}$ obtained from XRD and Rietveld refinement.

Movie S1. AIMD-simulated conformational dynamics of LAOC^{0b} during 20 ps at 600 K. The movie shows the rotational motion of LAOC^{0b} changing the Cl^F-Al-Cl^B dihedral angle through the staggered-eclipsed-staggered conformational twist.

Movie S2. AIMD-simulated conformational dynamics of LAOC^{0b} during 20 ps at 300 K. The movie shows the rotational motion of LAOC^{0b} changing the Cl^F-Al-Cl^B dihedral angle through the eclipsed-staggered- eclipsed conformational twist, which occurs less frequently compared to 600 K. The trimer is a part of the solid, while the other trimers were omitted for visibility.

Movie S3. Viscoplastic behavior of PLAOC^{0.3b}. PLAOC^{0.3b} powder turned into viscous solid above the melting point of the incorporated LiAlCl₄.